Thermodynamic Calculation and Characterization of Carbide Precipitation in Laser-Deposited Material for High-Speed Steel Alloy

Ali Jammal, Gang Wang, Hanbo Yang, Songge Yang, Yu Zhong, and Yiming Rong

The laser cladding of the T15 high-speed steel (HSS) was accomplished and its typical microstructure was determined. The microstructure characterization of the clad layer showed three phases of microstructure, planar, cellular and equiaxed growth zones. Electron probe micro-analyzer (EPMA) showed high content in alloying elements at the cellular and equiaxed zones that contained V, C, Cr and W. Further, the analysis at the inter-granular zone presented the highest concentration in elements such as Mo, Cr and W. This showed the presence of carbides which were identified as MCI and M_6C at the cellular zone, and M_7C_3 and $M_{23}C_6$ at the equiaxed and inter-granular zones. The precipitation characterization along the line starting from the substrate and passing through the clad layer identified the austenite matrix and revealed the fluctuation in the alloying elements content, where its amplitude and count increased while passing through the planar zone and hitting the equiaxed zone. Equilibrium phase diagram thermodynamic calculation proved the presence of MCI, M_6C and $M_{23}C_6$ which precipitated respectively as the solidification proceeded. The M_6C carbide was rich in Fe and W with the presence of V and Cr. MCI carbide had high content of C and V also with dissolved content of W and Cr. Finally, $M_{23}C_6$ carbide contained high amounts of W, Cr and Mo. Scheil–Gulliver simulation model showed the presence of M_6C and MCI similar to the equilibrium phase diagram results, additionally, two carbides were revealed and identified as M_7C_3 and MCII carbides. The $M_{23}C_6$ was absent from the Scheil–Gulliver model. This is due to the assumption that in the Scheil–Gulliver model, the solid stage has no diffusion, and the $M_{23}C_6$ was proved to precipitate in later stages of solidification as shown in the equilibrium phase diagram results. Finally, transmission electron microscopy (TEM) and x-ray diffraction (XRD) showcased the presence of the carbides predicted from the equilibrium phase diagram.

1. Introduction

Laser cladding is a novel additive manufacturing technique used to fabricate or repair components by depositing clad layers on a substrate. This process uses absorbed laser and is controlled by a CNC system to create a melt pool on the substrate while simultaneously injecting powder into the molten zone to form a deposited track (Ref 1–3). Lase cladding is compared to welding process with the ability to produce a strong bond between the substrate and the deposited material. With the provision of good process control, the sharp concentrated and low heat input provides a high precision material deposition (Ref 4). Furthermore, due to its processing advantages such as high-power density and material deposition rates, minimal dilution, low distortion and a strong joint between substrate and deposited material, laser cladding became a popular technique for industrial applications (Ref 5, 6).

High-speed steel (HSS) is considered a high alloy steel and the alloying elements percentage will range between 10 and 25%. These alloying elements will promote carbide formation upon solidification. This steel is presented as Fe-C-X, where X stands for elements leading to the carbide formation such as chromium, molybdenum tungsten and vanadium. HSS is used in applications requiring high strength and hardness, wear and corrosion resistance (Ref 7, 8). During steel solidification, the alloying elements will contribute to the formation of several types of carbides, e.g. MC, M_2C, M_6C, M_7C_3 and $M_{23}C_6$ (Ref 9, 10). The carbides type, shape, size, and distribution will directly affect the solidifying HSS mechanical properties. The carbides forming at the grain boundaries will usually have a coarse structure with a size ranging from 20 to 200 μm (Ref 11).

In application where powder injection is used, finer microstructure is expected to appear in the clad layer. Further, the solidification in this process is considered to be rapid, hence leading to superior mechanical properties (Ref 12, 13). It was reported that the M_2C will exist in steel containing tungsten and molybdenum, especially with increasing amount of carbon (Ref

Ali Jammal, State Key Laboratory of Tribology & Institute of Manufacturing Engineering, Department of Mechanical Engineering, Tsinghua University, Beijing 100084, China; and Department of Mechanical and Energy Engineering, Southern University of Science and Technology, Shenzhen 518055, China; **Gang Wang** and **Hanbo Yang**, State Key Laboratory of Tribology & Institute of Manufacturing Engineering, Department of Mechanical Engineering, Tsinghua University, Beijing 100084, China; **Songge Yang** and **Yu Zhong**, Department of Mechanical Engineering, Worcester Polytechnic Institute, Worcester, MA 01609; and **Yiming Rong**, Department of Mechanical and Energy Engineering, Southern University of Science and Technology, Shenzhen 518055, China. Contact e-mail: gwang@tsinghua.edu.cn.

14, 15). Though they are metastable at high temperature, during heat treatment this type of carbide will decompose along the γ-austenite matrix into MC and M_6C carbides at temperature exceeding 1000 °C (Ref 16). Other studies showed that during the casting of HSS alloys, nano-precipitates evolved and were identified as M_7C_3 and $M_{23}C_6$ (Ref 17, 18). For ultra-cooled solidifying HSS, as in the case of solidifying liquid melt in laser cladding process, studies showed the presence of an unidentified complex carbide structure rich with V, Mo, W, and Cr. The lattice spacing of the mentioned carbide ranged between 0.15 and 0.26 nm. This spacing is different from the usual reported carbide lattice spacing that tends to exist in HSS (Ref 19–21).

As previously presented, many studies addressed the carbide formation for larger specimen, as in casting process, whereas fewer research work addressed carbides in ultra-cooled environment such as in laser cladding where the deposited layer is relatively small and the deposited molten layer will solidify in seconds. Hence this study aimed to provide a comprehensive approach to identify the carbide formation in ultra-cooled T15 HSS. This provides a detailed insight on the microstructure and phase constitution of the cladding layer.

The in-depth characterization of carbide structure and distribution is formulated in different areas of the cladding layer. Initially thermodynamic calculation using equilibrium phase diagram and Scheil–Gulliver model were carried to predict the forming carbides. Then, many experimental procedures to identify the predicted carbides were used such as electron probe microscopy analysis (EPMA), scanning electron microscopy (SEM), and transmission electron microscope (TEM). The characterization process ranged from micro to nano-scale with the addition of identifying the carbides chemical composition.

2. Materials and Methods

In order to carry the laser cladding experiment, a 3 KW diode laser source (LDM3000-100) was used as it can be seen from Fig. 1. The minimum beam quality was equal to 20 mm mrad and the wavelength range was 900 to 1070 nm. The laser was equipped with a transport fiber having a core diameter of 1000 μm. In order to improve shielding characteristics, the nozzle was equipped by an extra shielding gas tube.
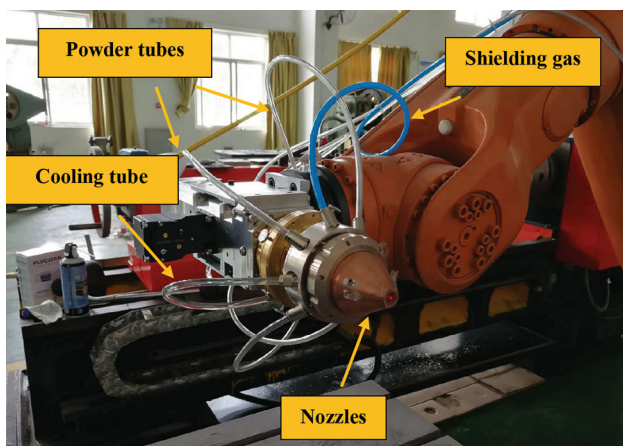

Fig. 1 Laserline diode laser source (LDM3000-100)

Hence, the injection head was equipped with 6 tubes in total, two tubes were for cooling and shielding gas, and the other four were for the powder and the carrier gas.

The laser beam was directed on the designated substrate in order to create the molten pool. The substrate material was 42CrMo steel. The powder was injected on the molten pool through four circumferentially equally spaced nozzles. The powder material was T15 steel (Fe_{bal-x}-C-Co_x-Cr-Mn-W-V-S), the cladding powder material was purchased with high percentage of carbide forming elements as V and W, the powder had spherical morphology, and the average particle size was equal to 70 μm. The T15 powder material was mixed with CeO_2 nano-powder having a mean diameter of 30 nm. The mixture percentage was 99 wt.% of T15 and 1 wt.% of CeO_2 powder. The addition of CeO_2 into the powder mix aim to deactivate the surface-active elements which are mainly deactivated by Ce. The following will affect the surface tension temperature coefficient resulting outward flow pattern in the molten pool compared to and inward flow for pure T15. This will reduce the segregation at the cladding layer surface.

The carrier gas was argon, the total flux was equal to 6 L/min. Further, argon was also used as a shielding gas, in order to prevent the molten pool from oxidization. The total flux of the shielding gas was equal to 20 L/min. Table 1 presents the material composition and alloying elements of the 42CrMo substrate and T15 powder.

A schematic of the single-track laser cladding experiment is presented in Fig. 2. Fig. 2(a) shows the cladding process with the laser scanning direction, the powder projection onto the substrate and solidifying clad layer. The substrate was static and fixed on the experimental rig. After conducting the experiment, the samples were cut using electrical discharge machining (EDM) where the dimension of the specimen was 1*1 cm including the clad layer. Then they were mechanically grinded and polished with Diamond suspension of 1, 0.5, and 0.25 μm. Finally, the microstructure was examined at transverse and longitudinal cross-sections using TEM and finally XRD analysis as shown in Fig. 2(b).

The cut samples were examined under Phenom desktop scanning electron microscope (SEM) in order to characterize the microstructure phases and evolution. Further, electron probe micro-analyzer (EPMA) was used to inspect the elements distribution at different microstructural structure. This experiment was carried using a JFOL jxa EPMA machine.

3. Microstructure Analysis

Laser trials were carried to produce ideal cladding layer formation and symmetricity. The feed rate was the parameter that controlled the dimension of the clad layer such as height. The laser power and the scanning speed and fee rate were set to be constants and fixed at 600 W, 6 mm/s and 3.6 g/min, respectively.

Table 1 Chemical composition of 42CrM0 substrate and T15 powder (wt.%)

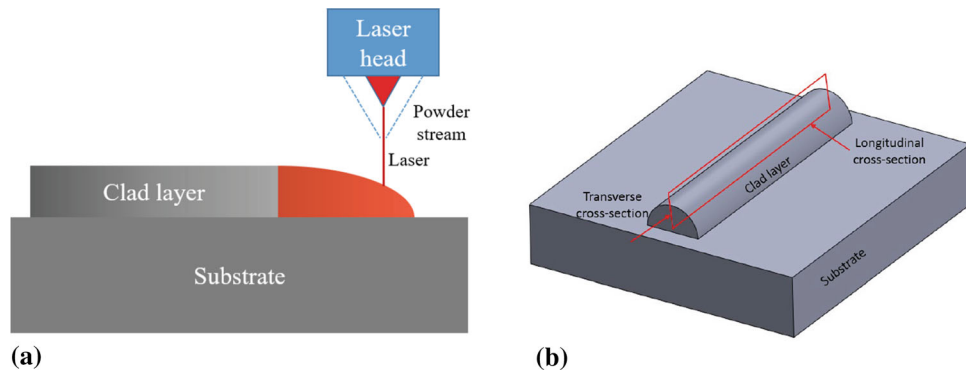| Material	C	Co	Cr	Mn	W	V	S	Fe
T15	1.60	5.00	4.00	0.3	12.9	4.9	0.04	Bal.
42CrMo	0.42	…	0.9	0.8	…	…	0.04	Bal.

Fig. 2 Schematic of laser hot-wire deposition and sample preparation procedure. (a) Laser deposition process (b) Inspected cross sections
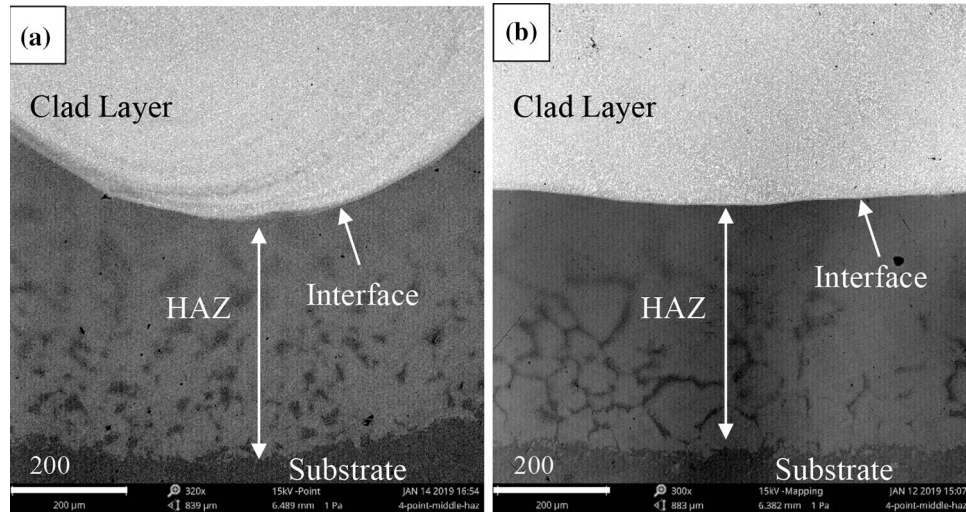

Fig. 3 SEM illustration of the cut sample. (a) Transverse cross-section (b) Longitudinal cross section

3.1 Microstructure Morphology Characterization

The SEM results of the cut sample cross-sections are shown in Fig. 3. Figure 3 A shows the microstructure at the transverse cross-section and Fig. 3(b) shows it at the longitudinal cross-section. It can be seen that the one clad layer deposited material has good formation quality with absence of cracks and minimal material defects. The interface between the clad layer and the substrate can be clearly seen, further the heat affected zone is also defined as shown below. The substrate–clad interface had circular shape at the transverse cross-section, and linear shape at the longitudinal cross-section.

The clad layer and substrate magnified microstructure are shown in Fig. 4. Fig. 4(a) and (b) shows a coarse and well-defined as-clad microstructure which can be divided into three phases of microstructure growth. This particular microstructural evolution is due to the high cooling rate of the laser cladding process. At the interface between the clad layer and the substrate, an initial planar growth took place which is due to the presence of the base metal or substrate. The existence of grains at the fusion zone provides the crystal nucleation during solidification, hence new crystals will form while having a certain crystallographic orientation and a cellular growth phase will appear. Finally, an equiaxed stage appeared and dominated the rest of the clad layer microstructure. Due to the ultra-high cooling rate and the relatively small clad layer size, the grains

size was almost uniform across the rest of the solidifying layer. Figure 4(c) shows a mgnification of the microstructure at the cellular and equiaxed zones. This revealed the presence of carbide formation at the grain boudary as well as at the austenite matrix. Spherical carbide were present at the inter-granular position (grain boundary) and some on the austenite matrix. Also, needle-like carbides were present at the inter-granular area of the equiaxed zone.

3.2 Alloying Material Composition

In order to inspect the alloying material composition in the clad layer, the sample were examined under an electron probe micro-analyzer. The test was repeated several times in order to verify the experiment reliability. The material characterization was carried at 4 points, where the first three points analyzed the material composition of the three stages of growth, at the planar, cellular and equiaxed growth zones. Finally, the fourth point was the inter-granular area at the growth interface of the equiaxed grains, as it can be seen from Fig. 5(a). The inter-granular zone was a subjected of interest because it is expected to have the higher probability for carbide formation, since it will have higher alloying material composition. Furthermore, the EPMA analysis was carried along a line starting from the substrate and passing through the different solidification stages as shown in Fig. 5(b).
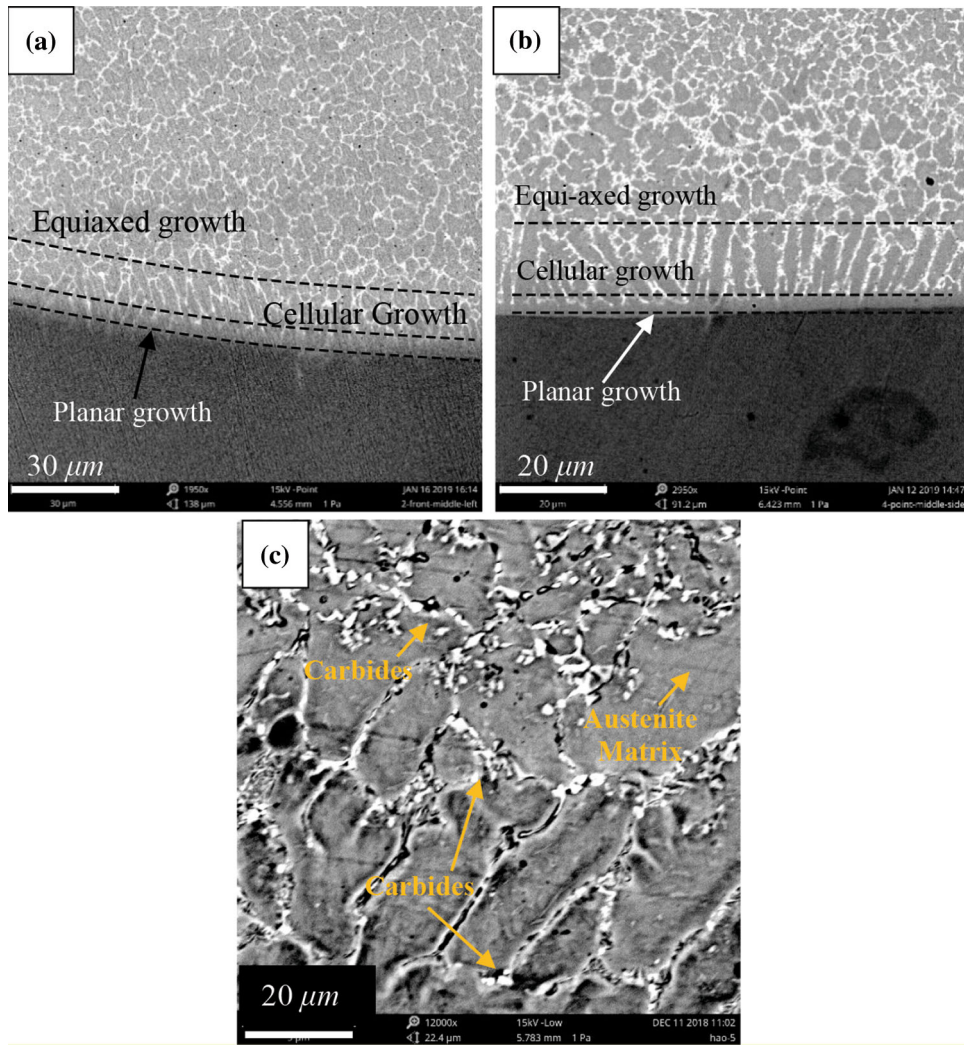
Fig. 4 SEM results of microstructure growth patterns and carbides distribution. (a) Transverse cross section (b) Longitudinal cross section (c) cellular and equiaxed zones
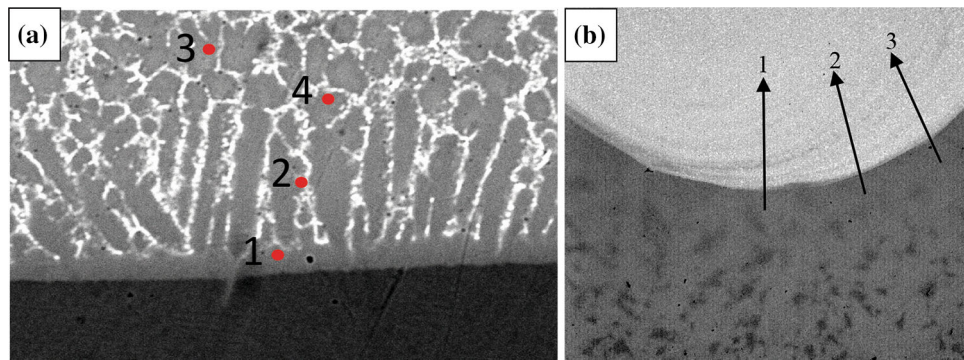

Fig. 5 EPMA material characterization at different analysis points. (a) (1) planar, (2) cellular, (3) equiaxed, (4) inter-granular (b) material characterization lines

The alloying materials weight percentage is shown in Table 2, the data were the average of the analysis points repetitive testing and error bars were introduced in Fig. 6 to highlight the measurement differences at each point. Table 2 shows the average weight percentage of all the alloys along with the Fe content. The Fe and Mo mass fraction were not included in Fig. 6 in order to produce a better representation of the alloying material at different inspection points. It can be seen from the graph below that the carbon concentration was around 1.5 wt.% in the planar zone that is roughly around the C wt.% in the HHS powder used in the cladding process. The C wt.% increased to reach 1.76 wt.% in the cellular growth zone,

Table 2 Material weight percentage at the selected points

Point	C	Fe	Co	W	Cr	V	Mn	Mo
1	1.495	82.168	3.681	6.336	2.892	0.314	0.440	0.059
2	1.762	80.382	4.556	7.107	3.204	0.547	0.400	0.039
3	2.131	79.035	4.861	7.431	3.422	0.601	0.371	0.024
4	5.811	54.421	2.957	26.980	7.891	0.393	0.524	0.244
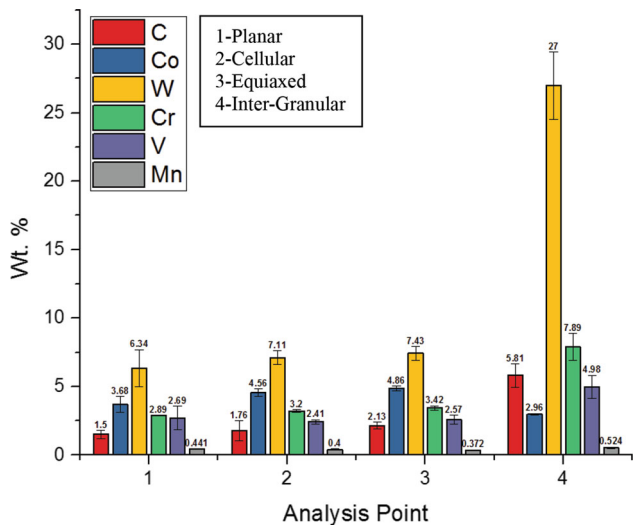
Fig. 6 EPMA Material weight percentage results

then it increased to reach 2.13 wt.% in the equiaxed zone. Finally, toward total solidification, the C wt.% reached it is highest and was equal to 5.81 wt.% in the inter-granular zone. Along C, other alloying carbides forming elements such as W, Cr and V are presented, as it can be seen from the graph below, W weight percentage was relatively high at points 1,2 and 3, it ranged between 6.34 to 7.43 wt.%, then it reached its highest at point 4 and was equal to 27 wt.%. Similarly, Cr weight increased gradually from point 1 to 3 then it hit 7.89 wt.% at point 4. However, V weight percentage was 2.69 wt.% at point one, then it decreased to 2.41 and 2.57 wt.% at points 2 and 3, then it increased to reach 4.98 wt.% at point 4. The Mn wt.% remained constant through the growth stages and Mo wt.% was low and negligible at points 1, 2 and 3, it reached its highest concentration at point 4.

The alloying elements analysis carried in transverse and longitudinal cross sections aims to present the material distribution trend that will lead to a better understanding on the carbide that might appear at different area of the clad layer. The material distribution showed a carbon weight at points 2 and 3 ranging between 1.76 and 2.13 wt.%, combined with Cr weight ranging between 3.2 and 3.42 wt.% and W weight ranging between 7.11 and 7.43 wt.%. It can be assumed that the carbides which will be present in those areas are identified as MC and M_6C rich in the aforementioned alloying elements. As for point 4 that represents the inter-granular zone, there was a high weight concentration of C, which reached 5.8 wt.%, and it had also the highest weight concentration of W equal to 27 wt.% and a weight concentration of Cr equal to 7.89 wt.%, and hence it is assumed that the carbide present in this zone are the M_7C_3 and $M_{23}C_6$ rich in carbon, chromium and mainly tungsten.

In order to ensure the accuracy and the repeatability of the EPMA test, line material characterization on multiple places in the clad layer was carried and the material distribution trend and uniformity are inspected and the sampling errors were nullified. Hence, it can be seen for Fig. 7 that the material distribution is consistent for each of the characterized material, and the alloying elements C, Cr and W concentration increased as the inspection line traveled from the substrate to the clad layer. On the other hand, the Fe concentration was higher at the substrate and declined in the clad layer.

A closer inspection on the analysis line 1 can be seen from the Fig. 8, initially the content of Fe was high since the Fe wt.% was higher in the substrate than the clad layer. The interface is identified as the doted red line between the substrate and the planar zone. The Fe content was almost constant in the planar zone with some fluctuation peaks in the carbide forming elements Cr and W. As for the cellular zone, the Fe peaks presents the austenite matrix and the C, Cr and W peaks present the inter-granular composition at the cellular grains. Hence the number of Fe peaks can be attributed to the number of grains in the analyzed zone along the line. The Cr and W peaks became more frequent with higher amplitude in the equiaxed zone, and this is due to the grain smaller size compared to cellular zone. The austenite matrix was highlighted by a black enclosing rectangle and the carbides were highlighted by red enclosing rectangles as it can be seen below.

The Cr and W content peaks recorded in the in the cellular zone indicated the presence of M_6C carbides as it can be seen from first highlighted carbide presence in Fig. 8 where the carbon peaked as well; however, its peak was lower in amplitude relative to its total content compared to Cr and W. Cr and W peaks were also present in equiaxed zone with higher intensity. Also, for the second highlighted carbide presence, Cr, W and C peaked in the equiaxed zone with an almost similar intensity which indicated the presence of M_7C_3 carbide. Finally, the third highlighted carbide presence showed the highest intensity peaks for Cr and W carbides, also C peaked with a relatively lower intensity, this indicated the presence of $M_{23}C_6$ carbide in that area. The MC carbide is hard to detect since it usually precipitates in the austenite matrix and the EPMA analysis line width did not cover enough area on the austenite matrix to detect the presence of the following carbide. It can be concluded that different carbides will be present at different growth stages as it can be seen from the aforementioned data, and as the solidification advanced the alloying elements content will become higher, leading to increased alloying element content in advanced stages of solidification such as in the equiaxed zone. Though the alloying element content increase is slight while the analysis line went from the cellular to equiaxed zone, the increase is noticeable for all alloying elements with the exception of Mn as shown in Fig. 6. Adding that the line analysis is not as accurate as the point analysis, which clearly
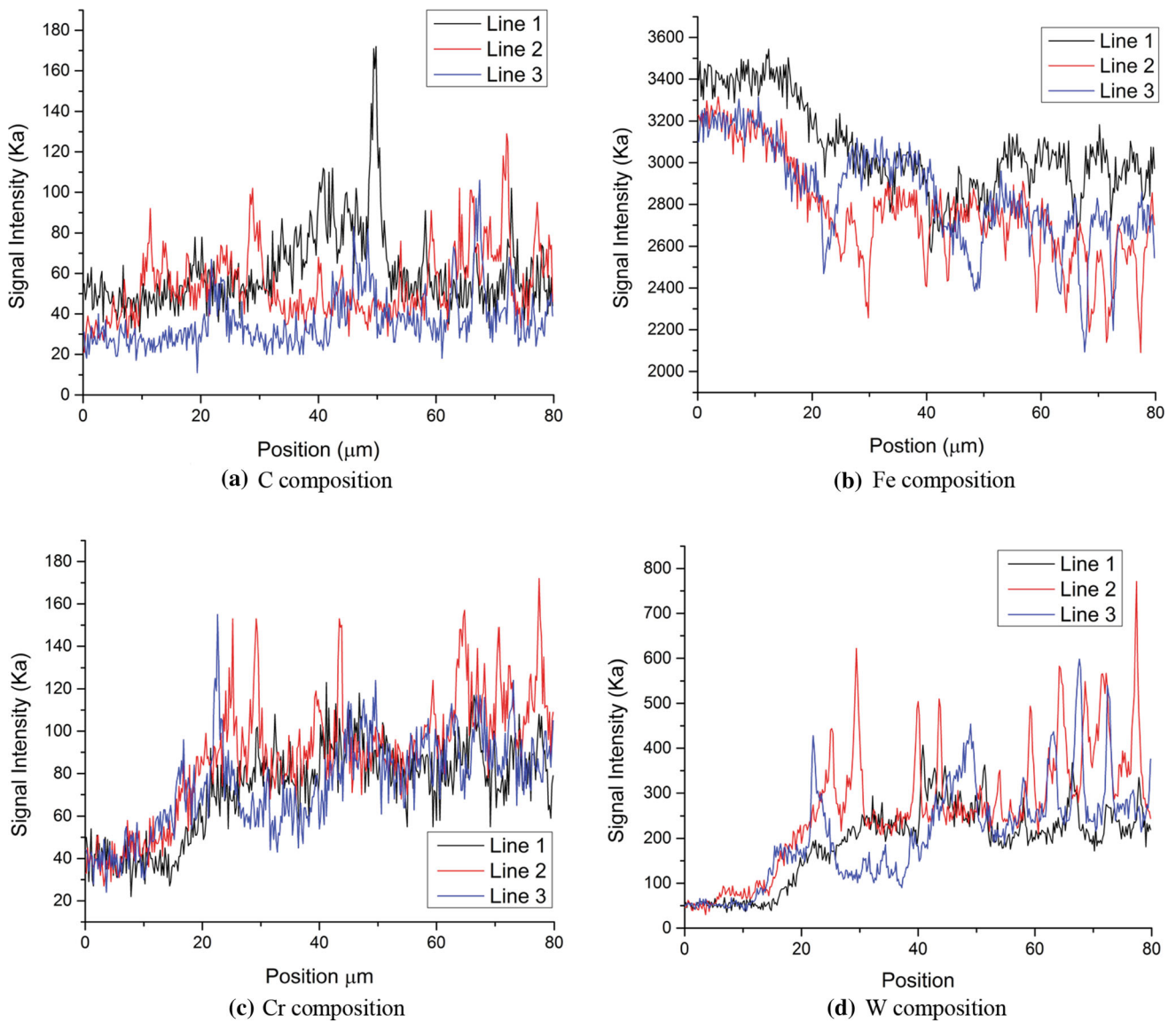
(a) C composition

(b) Fe composition

(c) Cr composition

(d) W composition

Fig. 7   EPMA signal intensity of C, Fe, Cr and W along the analysis lines presented in Fig. 5(b)
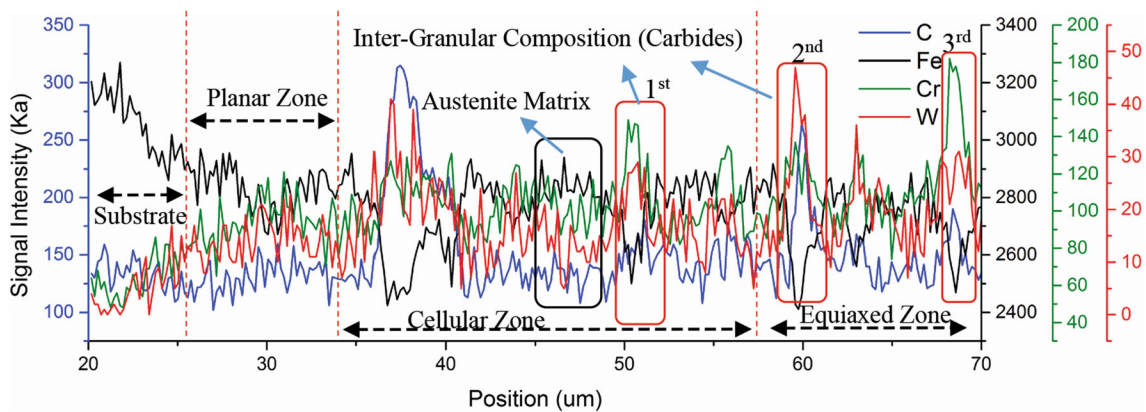

Fig. 8   EPMA signal intensity of C, Fe, Cr and W along the analysis line 1 presented in Fig.5(b)

shows that W content peaked with its highest amplitude at the inter-granular analysis point present in the equiaxed zone. The slight increase between the cellular and equiaxed zone can also be attributed to the short analysis line and the relatively small area where cellular zone is present.
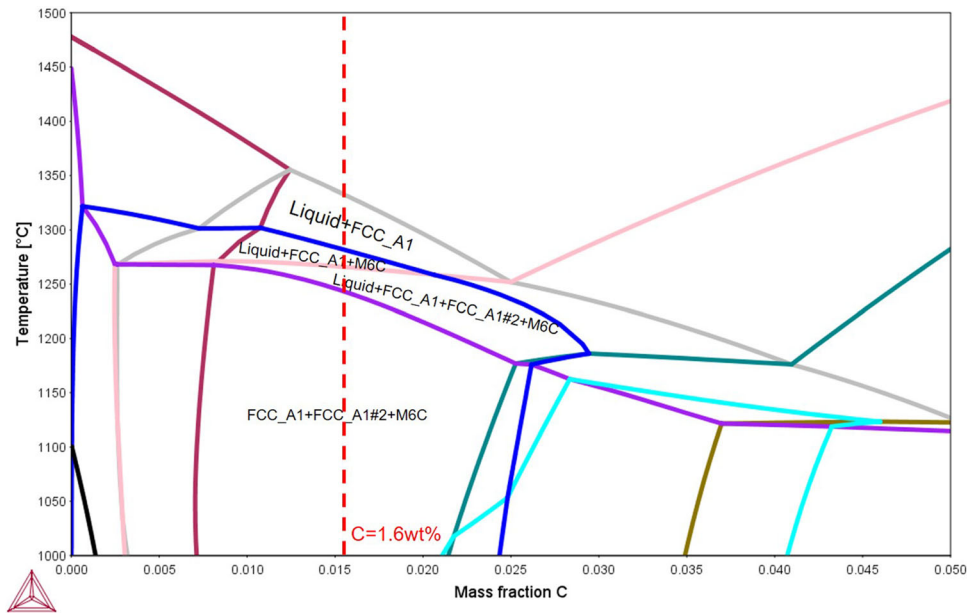
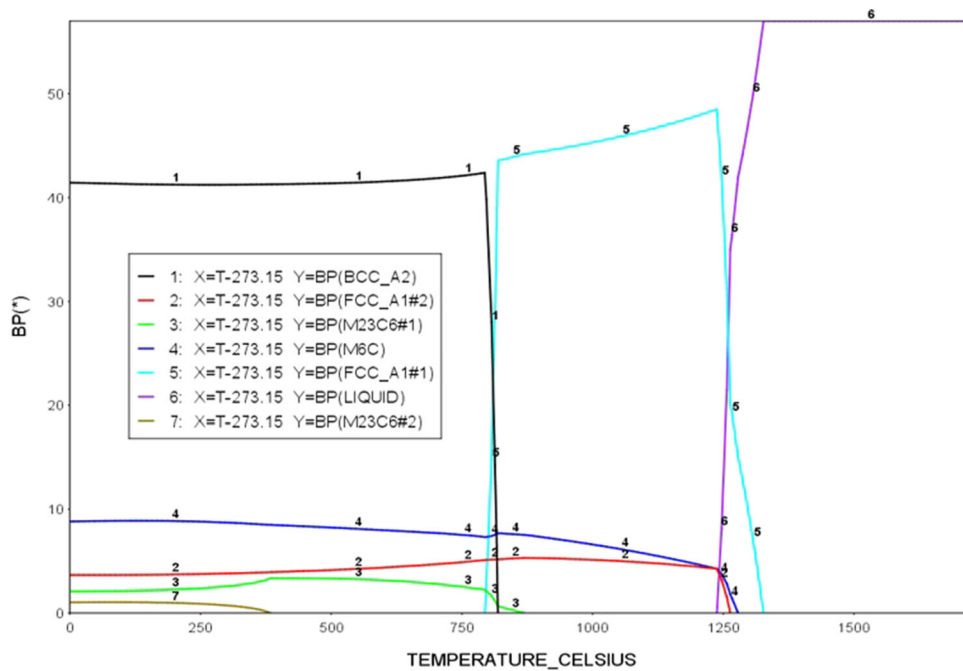**Fig. 9**   Isopleth phase diagram of the studied T15 HSS

Fig. 10   HSS phase mass fraction-temperature curve

4. Thermodynamic Calculation of the T15 HSS

4.1 Equilibrium Phase Diagram

The HSS Fe-C isopleths were simulated in Thermo-Calc software taking into consideration the alloying elements composition, the diagram is presented in Fig. 9. The carbon composition was equal to 1.6 wt.%, this was highlighted by the red dotted line sketched on the diagram. As it can be seen from the diagram below, the starting precipitation temperature of the austenite phase was 1330 °C and the precipitation temperature
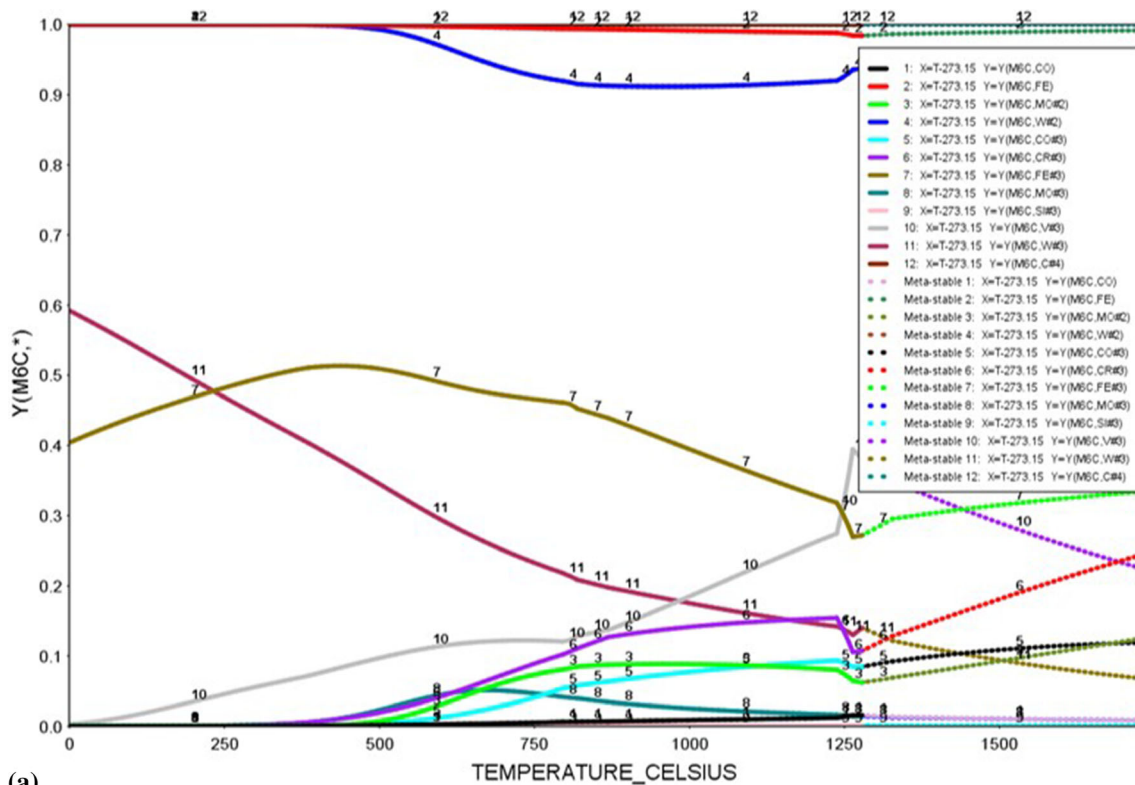
of the M_6C was 1278 °C. The precipitation temperature of MCI which is presented in Thermal-Calc software as FCC_A1#2 was 1264 °C. The solid stage along with the M_6C and MCI carbide started at temperature of 1243 °C.

The mass fraction variation with respect to temperature is show in Fig. 10. It can be seen that the austenite phase presented by line 5 starting at temperature of 1285 °C. Ferrite phase presented by line 1 started appearing at temperature equal to 798 °C. MCI, $M_{23}C_6$, M_6C were present and are presented by lines 2, 3 and 4, respectively. Another $M_{23}C_6$ phase appeared in later stage of cooling presented by line 7. The
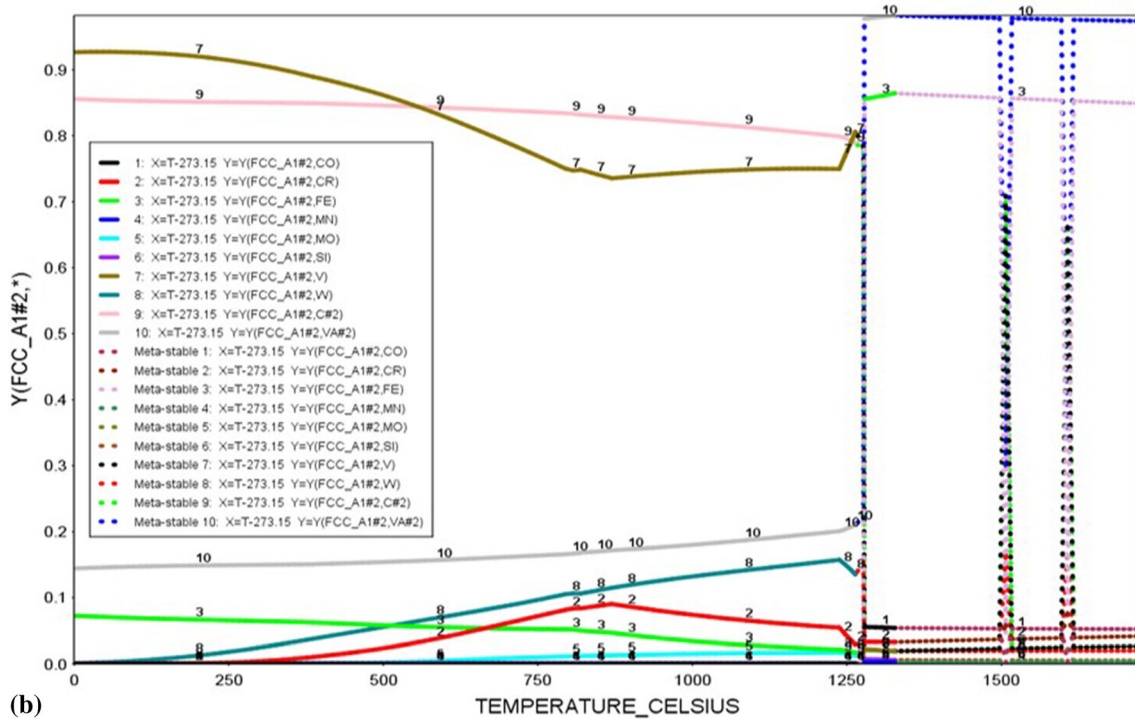
starting precipitation temperature and maximum mass fraction of carbides started after the decrease in austenite fraction.

The precipitation temperature of MCI carbide was 1274 °C, its mass fraction slightly decreased with temperature decrease. For $M_{23}C_6$ the starting precipitation temperature was equal to 871 °C, the mass fraction increased initially to its maximum then slightly decreased as the temperature decreased. Finally, M_6C precipitation temperature was equal to 1292 °C, its mass fraction increased gradually with the temperature decrease. The second $M_{23}C_6$ phase (line 7) precipitation temperature was equal to 383 °C with its mass fraction maximus remaining constant with the temperature decrease.

(a)

(b)

Fig. 11 Site fraction of carbide forming elements. (a) M_6C (b) MCI (c) $M_{23}C_6$

The legend (right side of figure):

- Meta-stable 1: X=T-273.15 Y=Y(M23C6#1,CO)
- Meta-stable 2: X=T-273.15 Y=Y(M23C6#1,CR)
- Meta-stable 3: X=T-273.15 Y=Y(M23C6#1,FE)
- Meta-stable 4: X=T-273.15 Y=Y(M23C6#1,MN)
- Meta-stable 5: X=T-273.15 Y=Y(M23C6#1,V)
- Meta-stable 6: X=T-273.15 Y=Y(M23C6#1,CO#2)
- Meta-stable 7: X=T-273.15 Y=Y(M23C6#1,CR#2)
- Meta-stable 8: X=T-273.15 Y=Y(M23C6#1,FE#2)
- Meta-stable 9: X=T-273.15 Y=Y(M23C6#1,MN#2)
- Meta-stable 10: X=T-273.15 Y=Y(M23C6#1,MO#2)
- Meta-stable 11: X=T-273.15 Y=Y(M23C6#1,V#2)
- Meta-stable 12: X=T-273.15 Y=Y(M23C6#1,W#2)
- Meta-stable 13: X=T-273.15 Y=Y(M23C6#1,C#3)
- 1: X=T-273.15 Y=Y(M23C6#1,CO)
- 2: X=T-273.15 Y=Y(M23C6#1,CR)
- 3: X=T-273.15 Y=Y(M23C6#1,FE)
- 4: X=T-273.15 Y=Y(M23C6#1,MN)
- 5: X=T-273.15 Y=Y(M23C6#1,V)
- 6: X=T-273.15 Y=Y(M23C6#1,CO#2)
- 7: X=T-273.15 Y=Y(M23C6#1,CR#2)
- 8: X=T-273.15 Y=Y(M23C6#1,FE#2)
- 9: X=T-273.15 Y=Y(M23C6#1,MN#2)
- 10: X=T-273.15 Y=Y(M23C6#1,MO#2)
- 11: X=T-273.15 Y=Y(M23C6#1,V#2)
- 12: X=T-273.15 Y=Y(M23C6#1,W#2)
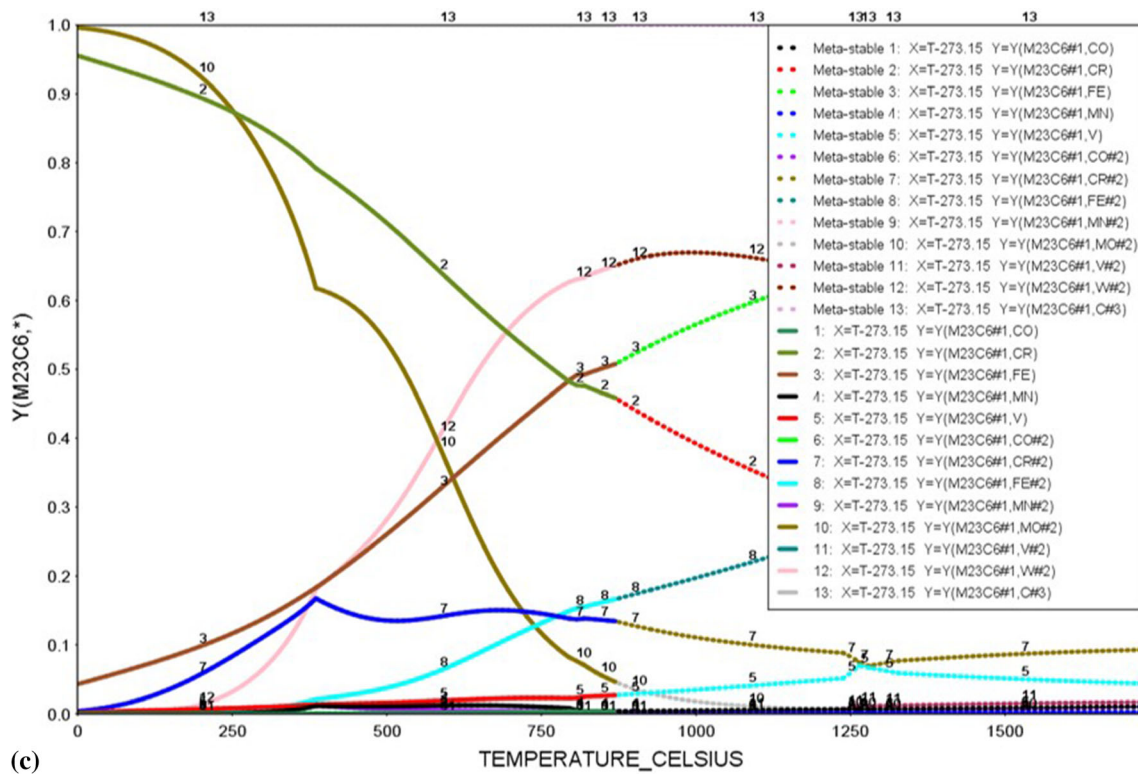- 13: X=T-273.15 Y=Y(M23C6#1,C#3)

(c)

Fig. 11 continued

The main alloying elements site fraction of the three different type carbides with respect to temperature variation are presented in Fig. 11. It can be seen that, for the first precipitated carbide, M_6C (Fig. 11a) contained high amount of elements Fe and W and it dissolved some amount of elements Cr and V. As for the second precipitated carbide, the MCI (Fig. 11b) contained high amount of the elements C and V, also it dissolved certain amounts of W, Cr and Fe. Finally, for the last precipitated carbide, the $M_{23}C_6$ (Fig. 11c) contained high amounts of Cr, W and Mo, it also dissolved certain amount Fe.

It can be concluded that the thermodynamic calculation is consistent with the EPMA results carried of the different solidification zone presented in the previous section. At points two and three which presents the cellular and equiaxed growth zones, the EPMA results showed the presence of V, C, Cr and W alloying elements concentration, this led to the assumption of the presence of MCI and M_6C carbides, and from the thermodynamic simulation it can be seen that the first precipitated carbide M_6C had high amount of W with dissolving amount of V and Cr. Further, for the second precipitated carbide MCI, the thermodynamic simulation showed that it had high amounts of the elements C and V with some dissolving amount of W and Cr which is consistent with the EMPA analysis results. For the EPMA analysis, point 4 representing the inter-granular position at the equiaxed stage, showed high amount of elements W, Cr and Mo. This result was consistent with thermodynamics findings of the $M_{23}C_6$ carbide alloying element content presented in Fig. 11(c), where is showed that this carbide precipitates in later stages of solidification and is rich in the same elements W, Cr, and Mo.

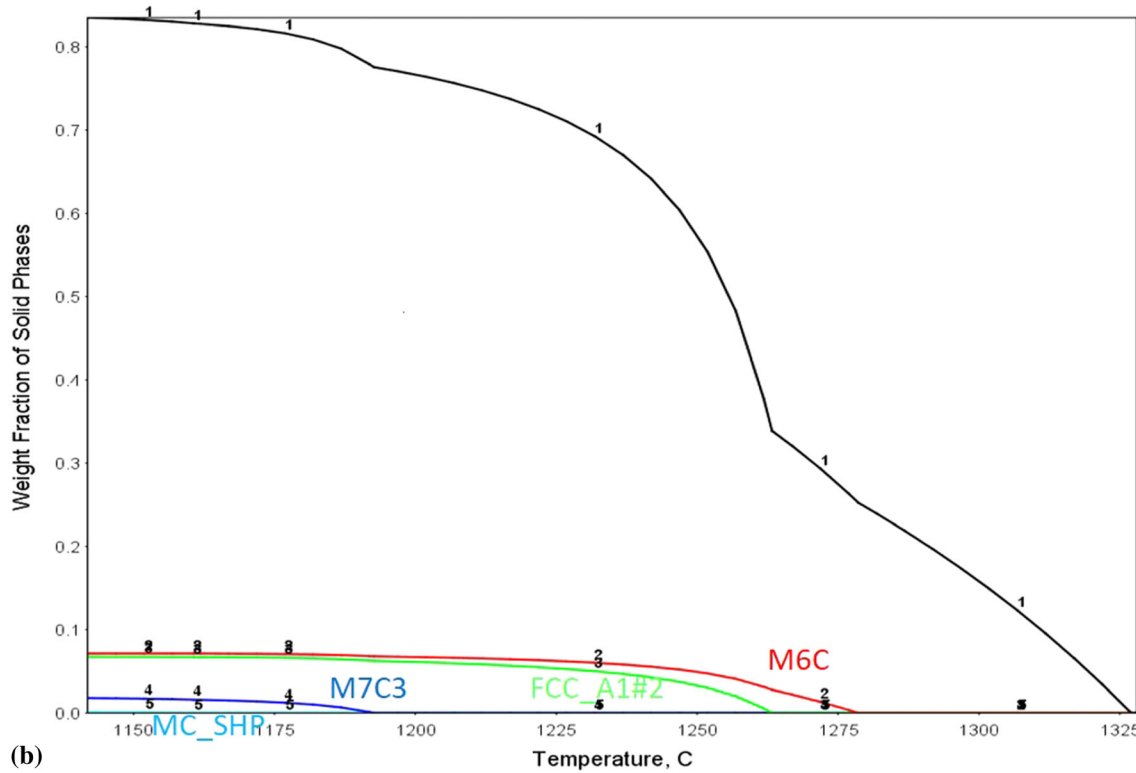## 4.2 Scheil–Gulliver Simulation

In order to gain a better insight into the carbide formation, and since in laser cladding, high cooling rate is subjected to the clad layer, Scheil–Gulliver model is employed to analyze the carbides evolution in the solidifying layer. Scheil–Gulliver model is often used to study solidifying alloy under non-equilibrium conditions. It provides a more accurate approximation of the solute segregation compared to equilibrium lever rule. Further, it assumes that there is no diffusion in the solid phase in order for the liquid composition to follow the liquidus temperature represented by the equilibrium phase diagram. Figure 12(a) presents the molar fraction of solid phases and the precipitation temperature of each phase. Also, Fig. 12(b) shows the weight fraction of each phase. It can be seen from Fig. 12(a) the presence of the following carbides: M_6C, MCI, M_7C_3 and MCII referred as MC_SHP in thermal-Calc.

As it can be seen for M_6C and MCI the precipitation temperatures were 1278 and 1264 °C respectively, this was similar to the precipitation temperature of those carbide calculated in the equilibrium phase diagram from the previous section. Two new carbides appeared in Scheil–Gulliver simulation model, the M_7C_3 and MCII carbides having the same precipitation temperature equal to 1192 °C.

When compared to the equilibrium phase diagram, Scheil–Gulliver model also predicted the precipitation of MCI and M_6C type carbides that will appear at early stages of solidification. Furthermore, two new carbides appeared which were M_7C_3 and MCII type carbides, the precipitated shortly after the appearance of MCI and M_6C. This is due to the Scheil–Gulliver model properties assuming that the solid stage has no diffusion, hence as the solidification proceeds, the alloying elements will not precipitate in the solid part. This will
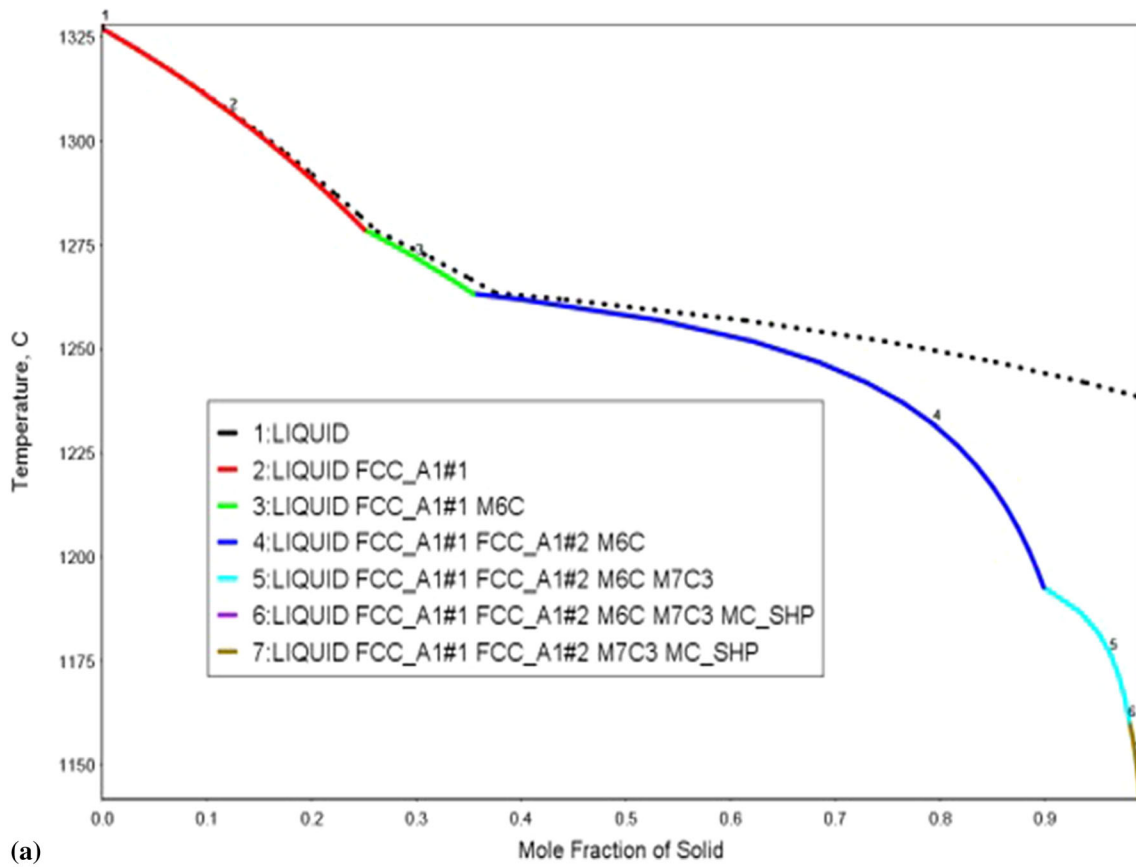
Fig. 12 Scheil–Gulliver model Mole and weight fractions variation with respect to temperature. (a) Mole Fraction (b) Weight fraction
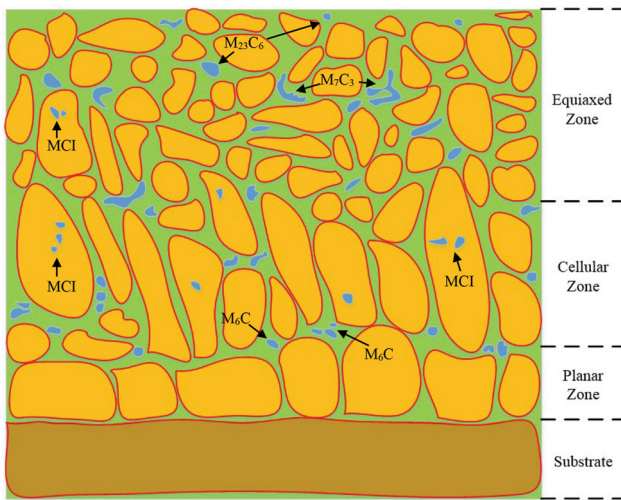
Fig. 13 Illustration of the different solidification zones with their respective carbides structure and distribution

Table 3 Carbides precipitation temperature

Analysis model	M_6C	MCI	M_7C_3	MCII	$M_{23}C_6$
Equilibrium phase diagram	1278	1264	N/A	N/A	870
Scheil–Gulliver model	1278	1264	1192	1192	N/A

increase the content of the alloying elements in the liquid phase, hence M_7C_3 and MCII carbides rich in elements such as W and Cr appeared. As shown from the equilibrium phase diagram before, $M_{23}C_6$ will precipitate in later stages of solidification, hence this carbide was absent from the Scheil–Gulliver simulation due to the fact that after total solidification, the diffusion will not proceed in the solid stage.

5. Discussion

Figure 13 is a representative schematic of microstructure resulting from the laser cladding of HSS studied in this paper. The presented microstructures were the planar, cellular and the equiaxed zones. As it can be seen, the carbides formed at the inter-granular zones and some were present at the austenite matrix. Granular and needle like carbides at the grain boundaries and in the austenite matrix were identified. Table 3 shows the precipitation temperature of the carbides identified by the equilibrium phase diagram and the Scheil–Gulliver model. The starting microstructure consisted of small granular M_6C carbide at the grain boundaries of the cellular zone as it can be seen from Fig. 13 the following can be concluded from the EPMA and site fraction results showing that area is rich in W and Cr and from the fact that M_6C had the highest precipitation temperature.

The second precipitated carbide was the MCI, having a slightly lower precipitation temperature compared to M_6C, the following carbide is known to precipitate in the austenite matrix (Ref 22). Further, it is rich in C and V which was shown in the analysis of points 2 and 3 of the EPMA and from the

equilibrium phase diagram site fraction results. The MCI carbide is highlighted in figure below.

The last precipitating carbides were identified as M_7C_3 and $M_{23}C_6$ which appeared at the grain boundaries of the equiaxed zone. They hold the lowest precipitation temperature as shown in Table 3. The presence of $M_{23}C_6$ was predicted form the equilibrium phase diagram analysis and Scheil–Gulliver model predicted the presence of M_7C_3. The M_7C_3 and $M_{23}C_6$ carbides are rich in Cr, W and C. Hence, the EPMA results at point 4 showed the presence of those carbides. As it can be seen in Fig. 13 the granular smaller carbides were identified as $M_{23}C_6$ as they tend to form as small spherical like grains along the grain boundary (Ref 23, 24). Also, usually carbides will form a cluster of different type of carbides, hence clusters of carbides can be seen for M_6C and $M_{23}C_6$. Finally, the M_7C_3 was identified as needle-like carbides which were dispersed along the grain boundary and also formed clusters at some certain areas (Ref 24, 25).

Scheil–Gulliver model predicted the precipitation of MCII, however, as it can be noticed from the weight fraction of each carbide presented in Fig. 12, its weight fraction in the solid phase is negligible. Adding that it is hard to index smaller amount of carbides in the EPMA and SEM analysis, hence the following carbide was not identified.

In order to verify the predicted carbides that will be present in the clad layer after the laser cladding process, scanning transmission electron microscopy (TEM) is carried and the carbides morphology and selected area diffraction patterns (SADP) are presented in Fig. 14. The carbide presented in Fig. 14a is identified as MCI, which will be present on the inside of the Fe matrix. The carbide presented in Fig. 14(b) is identified as $M_{23}C_6$ having a relatively small size and round shape spawning at the grain boundary. The carbide cluster shown in Fig. 14(c) is identified as M_7C_3 and finally the carbide presented in Fig. 14(d) is identified as M_6C which appeared at the grain boundary. As anticipated by the EPMA material characterization and phase diagram analysis, the TEM verified the presence of the predicted carbides in the Fe matrix and at the grain boundary.

Figure 15 shows the XRD results of the deposited track. The main precipitated phases were MCI, M_6C and $M_{23}C_6$ carbides. The XRD results did not detect the presence of M_7C_3 and MCII carbides, this is can be attributed to their low weigh fraction as it can be seen from the Scheil–Gulliver model simulation presented in Fig. 12.

6. Conclusion

The microstructure of T15 high-speed steel used in the laser cladding experiment was studied and characterized. The different alloying elements at different microstructural phases were inspected and the carbides types were predicted. The relationship between the microstructural phase and carbides alloying elements content was established. The alloying elements evolution starting from the substrate and passing over the clad layer was recorded and analyzed. The thermodynamic simulation on the T15 HSS was accomplished and the predicted carbide types were verified. Several conclusions can be drawn as follows:
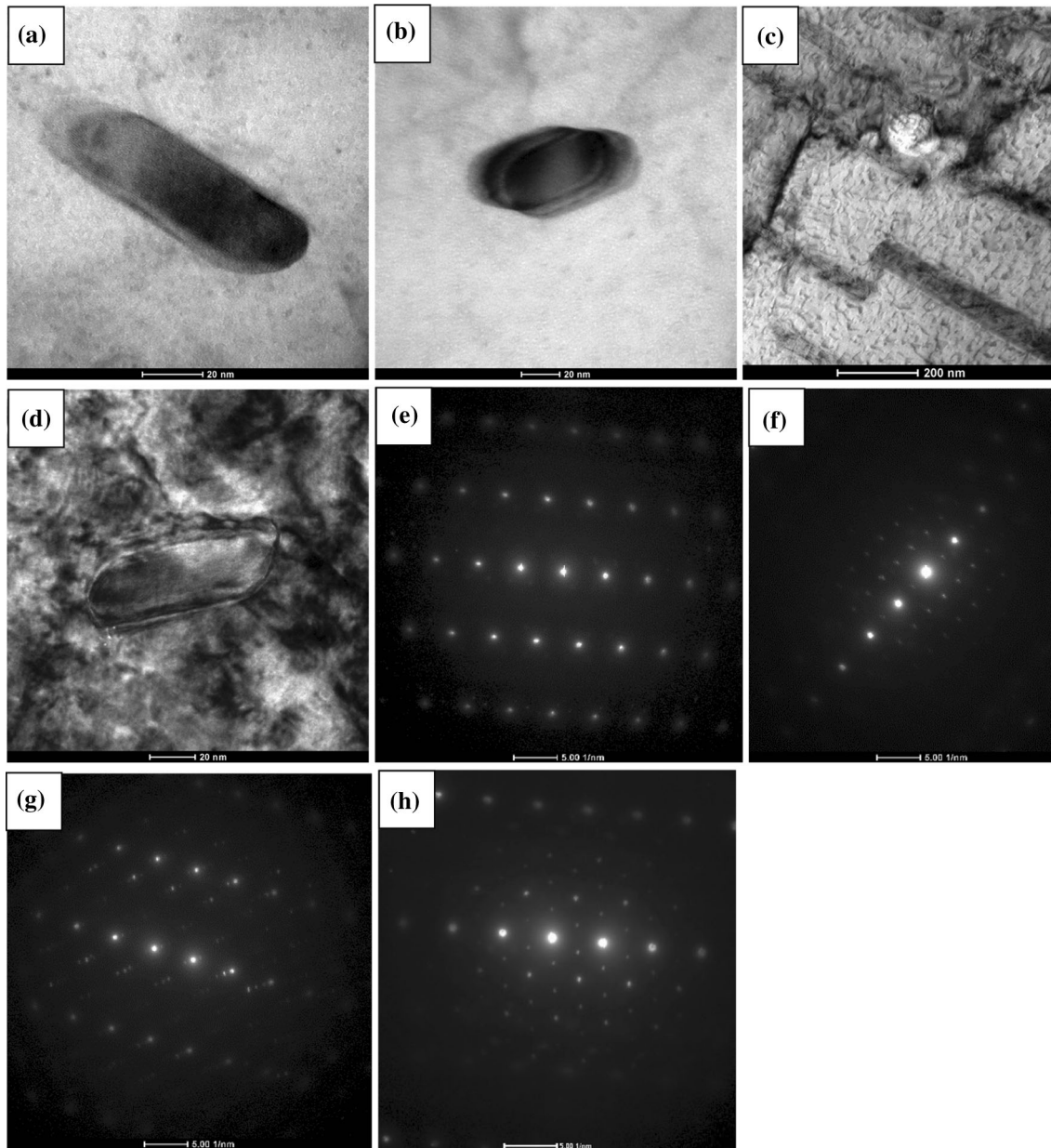
Fig. 14 Fine precipitates after laser cladding: (a) MCI in a bright field (BF) image from scanning transmission electron microscopy (TEM), (b) $M_{23}C_6$ in a TEM BF image, (c) M_7C_3 in a TEM dark field (DF) image, (d) M_6C in a TEM DF, (e) SADP of MCI in (a), (f) SADP of $M_{23}C_6$ in (b), (g) SADP of M_7C_3 in (c), and (h) SADP of M_6C in (d)

1. The alloying element analysis in the cellular and equiaxed zones showed relatively high concentration of C, Cr, W and V which indicated the presence of MCI and M_6C carbides. Similarly, the alloying element analysis at the inter-granular zone showed the highest concentration in W and Cr which indicated the presence M_7C_3 of $M_{23}C_6$ carbides.
2. The alloying elements characterization along the line starting from the substrate and passing through the clad layer showed the presence of carbides alloying elements in the austenite matrix and the inter-granular zones. Also, it indicated an increase in alloying element content as the analysis line hit the interface and proceeded into the clad layer, where the amplitude peaks hit their highest in the inter-granular zone.
3. HSS equilibrium phase diagram showed three type of carbides which precipitated respectively and were M_6C, MCI and $M_{23}C_6$. The elements site fraction of the carbides showed that M_6C contained a relatively high amount of W and Fe, the MCI carbide had high content of C and V, and the $M_{23}C_6$ carbide contained the highest content in Cr, W, and Mo. The thermodynamic simulation verified the carbides predicted in the previous experimental section, with the only carbide absent from the equilibrium phase diagram being the M_7C_3.
4. The Scheil–Gulliver simulation model revealed the presence of four carbides type identified as M_6C, MCI, M_7C_3 and MCII which precipitated, respectively, with the decrease in temperature. Similar to the equilibrium phase diagram, Scheil–Gulliver model predicted the precipita-
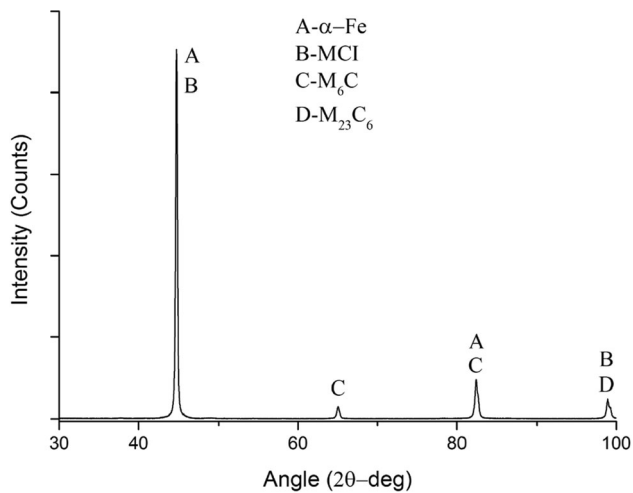
Fig. 15 Laser cladding deposited track XRD results

tion of M_6C and MCI. However, it predicted the precipitation of the two additional carbides M_7C_3 and MCII. Further, this model indicated that the $M_{23}C_6$ will not precipitate, this is due to the assumption of the Scheil–Gulliver that there is no diffusion in the solid state, and the $M_{23}C_6$ will precipitate the latest as shown in the equilibrium phase diagram.

5. TEM results showed that the predicted carbides were present in the clad layer where all the carbides are identified with the exception of MCII carbide. Similarly, XRD results predicted the presence of MCI, M_6C and $M_{23}C_6$ carbides, however M_7C_3 and MCII were not detected due to their low weigh fraction.

Acknowledgments

References

1. L. Dubourg and J. Archambeault, Technological and Scientific Landscape of Laser Cladding Process in 2007, *Surf. Coat. Technol.*, 2008, **202**(24), p 5863–5869
2. W. Gao, Y. Zhang, D. Ramanujan, K. Ramani, Y. Chen, C.B. Williams, C.C.L. Wang, Y.C. Shin, S. Zhang and P.D. Zavattieri, The Status, Challenges, and Future of Additive Manufacturing in Engineering, *Comput. Aided Des.*, 2015, **69**, p 65–89
3. S.M. Thompson, L. Bian, N. Shamsaei and A. Yadollahi, An Overview of Direct Laser Deposition for Additive Manufacturing; Part I: Transport Phenomena, Modeling and Diagnostics, *Addit. Manuf.*, 2015, **8**, p 36–62
4. J. Dowden, *The Theory of Laser Materials Processing*, Springer, Amsterdam, 2009, p 235–236
5. E.M. Birger, G.V. Moskvitin, A.N. Polyakov and V.E. Arkhipov, Industrial Laser Cladding: Current State and Future, *Weld. Int.*, 2011, **25**(3), p 234–2436
6. S. Liu, W. Liu, M. Harooni, J. Ma and R. Kovacevic, Real-Time Monitoring of Laser Hot-Wire Cladding of INCONEL 625, *Opt. Laser Technol.*, 2014, **62**, p 124–134
7. H.T. Phan, A.K. Tieu, H. Zhu, B. Kosasih, Q. Zhu, A. Grima and T.D. Ta, A Study of Abrasive Wear on High Speed Steel Surface in Hot Rolling by Discrete Element Method, *Tribol. Int.*, 2017, **110**, p 66–76
8. H. Tang, H. Zhang, L. Chen and S. Huo, Novel Laser Rapidly Solidified Medium-Entropy High Speed Steel Coatings with Enhanced Hot Wear Resistance, *J. Alloys Compd.*, 2019, **772**, p 719–727
9. K.C. Hwang, S. Lee and H.C. Lee, Effects of Alloying Elements on Microstructure and Fracture Properties of Cast High Speed Steel Rolls Part II. Fracture behavior, *Mater. Sci. Eng. A*, 1998, **254**, p 282–295
10. H. Qu, B. Liao, L. Liu, D. Li, J. Guo, X. Ren and Q. Yang, Precipitation Rule of Carbides in a New High Speed Steel for Rollers, *Calphad*, 2012, **36**, p 144–150
11. M. Boccalini and H. Goldenstein, Solidification of High Speed Steels, *Int. Mater. Rev.*, 2001, **46**, p 92–115
12. M. Nilsson and M. Olsson, Microstructural, Mechanical and Tribological Characterisation of Roll Materials for the Finishing Stands of the Hot Strip Mill for Steel Rolling, *Wear*, 2013, **307**(1–2), p 209–217
13. K.H. Lee, S.W. Choi, J. Suh and C.Y. Kang, Effect of Laser Power and Powder Feeding on the Microstructure of Laser Surface Alloying Hardened H13 Steel Using SKH51 Powder, *Mater. Des.*, 2016, **95**, p 173–182
14. P. Ding, G. Shi and S. Zhou, A Scanning Electron Microscopy Study of Carbides in High-Speed Steels, *Mater. Charact.*, 1992, **29**, p 15–24
15. Y.J. Li, Q.C. Jiang, Y.G. Zhao and Z.M. He, Behavior of Aluminum in M2 Steel, *Scr. Mater.*, 1997, **37**(2), p 173–177
16. F.S. Pan, W.Q. Wang, A.T. Tang, L.Z. Wu, T.T. Liu and R.J. Cheng, Phase Transformation Refinement of Coarse Primary Carbides in M2 High Speed Steel, *Prog. Nat. Sci. Mater. Int.*, 2011, **21**(2), p 180–186
17. A.J. Novinroozal, S. Moniri, M.A. Asadabad and A. Hojabri, The Study of Nano-Sized Carbide Particles Formed in Fe-Cr-W-V Alloy, *J. Mater. Eng. Perform.*, 2011, **21**(7), p 1440–1446
18. M.A. Asadabad, S. Kheirandish and A Novinrooz, Identification of Nanometric Carbide Precipitates in Fe-Cr-W-V System. Synth. React. Inorg. Met. Org. 2009, **39**(6), p 322–326
19. N. Ur Rahman, L. Capuano, A. van der Meer, M.B. de Rooij, D.T.A. Matthews, G. Walmag, M. Sinnaeve, A. Garcia-Junceda, M. Castillo and G.R.B.E. Römer, Development and Characterization of Multilayer Laser Cladded High Speed Steels. Addit. Manuf. 2018, **24**, p 76–85
20. N. Ur Rahman, M.B. de Rooij, D.T.A. Matthews, G. Walmag, M. Sinnaeve and G.R.B.E. Römer, Wear Characterization of Multilayer Laser Cladded High Speed Steels. Tribol. Int. 2019, **130**, p 52–62
21. S. Wei, G. Wang, J. Yu and Y. Rong, Competitive Failure Analysis on Tensile Fracture of Laser-Deposited Material for Martensitic Stainless Steel, *Mater. Des.*, 2017, **118**, p 1–10
22. X.F. Zhou, D. Liu, W.L. Zhu, F. Fang, Y.Y. Tu and J.Q. Jiang, Morphology, Microstructure and Decomposition Behavior of M2C Carbides in High Speed Steel, *J. Iron Steel Res. Int.*, 2017, **24**(1), p 43–49
23. R. Choteborsky, P. Hrabě, M. Müller, J. Savkova and M. Jirka, Abrasive Wear of High Chromium Fe-Cr-C Hard Facing Alloys, *Res. Agric. Eng.*, 2008, **54**, p 192–198
24. S. Liu, Y. Zhou, X. Xing, J. Wang, X. Ren and Q. Yang, Growth characteristics of Primary M_7C_3 Carbide in Hypereutectic Fe-Cr-C Alloy, *Sci. Rep.*, 2016, **6**(1), p 32941
25. M. Zhang, C. Chen, L. Qin, K. Yan, G. Cheng, H. Jing and T. Zou, Laser Additive Manufacturing of M2 High-Speed Steel. Mater. Sci. Technol. 2017, **34**(1), p 1–10